Astronomy & Astrophysics manuscript no. ms-2012-03-24˙age
April 2, 2012

Determination of the Acceleration Region Size in a Loop-structured Solar Flare

Jingnan Guo⋆[1], A. Gordon Emslie[2], Eduard P. Kontar[3], Federico Benvenuto[1], Anna Maria Massone[4], and Michele Piana[1,4]

(1) Dipartimento di Matematica, Università di Genova, via Dodecaneso 35, 16146 Genova, Italy
(2) Department of Physics and Astronomy, Western Kentucky University, Bowling Green, KY 42101, USA
(3) School of Physics and Astronomy, SUPA, University of Glasgow, Glasgow, G12 8QQ, Scotland
(4) CNR - SPIN, via Dodecaneso 33, I-16146 Genova, Italy

ABSTRACT

Aims. In order to study the acceleration and propagation of bremsstrahlung-producing electrons in solar flares, we analyze the evolution of the flare loop size with respect to energy and time. A GOES M3.7 loop-structured flare taking place at 23:55 on 2002 April 14 is studied in detail using *Ramaty High Energy Solar Spectroscopic Imager* (*RHESSI*) observations.
Methods. We construct photon and mean electron flux maps in 2-keV energy bins through the processing of observationally-deduced photon and electron visibilities, respectively, and by means of several image-processing methods: a visibility-based forward-fit (FWD) algorithm, a maximum entropy (MEM) procedure and the uv-smooth (UVS) approach. We estimate the sizes of elongated flares (i.e., the length and width of flaring loops) by calculating the second normalized moments of the intensity in any given map. Employing a collisional model with an extended acceleration region, we fit the loop lengths as a function of energy in both the photon and electron domains.
Results. The resulting fitting parameters allow us to estimate the extent of the acceleration region which is between ~ 15 arcsec and ~ 20 arcsec. Both forward-fit and uv-smooth algorithms provide substantially similar results with a systematically better fit in the electron domain.
Conclusions. The consistency of the estimates from both methods strongly suggests that the proposed model is reliable in determining geometric parameters of the acceleration region. The acceleration region is estimated to be a substantial fraction ($\sim 2/3$) of the loop extent, indicating that this dense flaring loop incorporates both acceleration and transport of electrons, with concurrent thick-target bremsstrahlung emission.

Key words. Sun: flares — Acceleration of particles

1. Introduction

Solar flares are known to produce large quantities of accelerated particles, in particular electrons in the deka-keV to deci-MeV range. However, the location and physical properties of the acceleration region are yet to be well constrained. An intrinsic complication is that the radiation produced by energetic particles emanates not only from the acceleration region itself, but also from other locations in the flare into which the accelerated particles propagate. Indeed, the oft-used "thick-target" model (Brown 1971) exploits this very complication by deriving properties of the hard X-ray emission that are completely independent of the location, extent, or physical properties of the acceleration region. Hence, determination of the properties of the acceleration region from spatially-integrated observations of flare emission is not straightforwardly possible. The reader is referred to recent reviews on electron properties inferred from hard X-rays (Kontar et al. 2011a) and their implications for electron transport (Holman et al. 2011).

With the availability of high-quality hard X-ray imaging spectroscopy data from the *RHESSI* instrument (Lin et al. 2002), the situation has much improved (see, e.g., Emslie et al. 2003). Higher energy electrons are able to propagate further from the acceleration region and hence produce hard X-ray emission over a greater spatial extent than in lower-energy bands. Xu et al. (2008) and Kontar et al. (2011b) analyzed a set of events characterized by simple coronal flare loop sources located near the solar limb. In order to determine the spatial properties of the flare loops they fitted the *RHESSI* visibilities with the geometric parameters of the loops and determined the size of the acceleration regions by fitting the source extents as a function of the photon energy with a collisional acceleration and propagation model.

The present paper extends this kind of analysis. Specifically, for the simple coronal loop event observed by RHESSI on 2002 April 14, we study the variation of source extent with energy not only in the *photon* energy domain, but also, for the first time, in the *electron* domain, using the procedure for generating weighted mean electron flux maps first enunciated by Piana et al. (2007). This extension of the model to the electron domain not only admits a simpler description of the source size with energy E; it also allows us to exploit the "rectangular" nature of the spectral inversion process, making

⋆ guo@dima.unige.it

it possible to reconstruct the electron maps at energies higher than the maximum photon energy observed. Moreover, the regularization algorithm used to invert count visibilities into electron visibilities introduces a natural smoothing constraint with energy E, which leads to a smoother behavior of source size with energy and so a more reliable estimate of pertinent parameters such as the acceleration region length.

From both photon and electron maps in a given time interval, we extract the form of the variation of loop length with energy. We have demonstrated that our approach to image reconstruction in the electron domain is made possible using electron visibilities; consequently, in this analysis we employ only visibility-based imaging algorithms for both photon and electron maps using three different imaging methods: visibility forward-fit (Schmahl et al. 2007), maximum entropy (Bone et al. 2007), and uv-smooth (Massone et al. 2009) procedures. In the visibility-forward-fit procedure, the loop sizes are determined as model parameters. For the other methods, we use the standard deviation – square root of the second normalized moment – of the intensity to construct the loop length. For each time interval we determine the loop length as a function of energy (both photon energy ϵ and electron energy E). We then use the model of Xu et al. (2008) to derive the physical properties of the acceleration and propagation regions, in particular the longitudinal and lateral extents of the acceleration site. In Section 2, we describe the inversion algorithms used to derive electron flux visibilities and the imaging techniques employed to create the corresponding electron maps for a given time interval and electron energy range. In Section 3, we fit the variation of loop size with electron energy E to a simple parametric model (Xu et al. 2008) in order to determine the extent of the acceleration region. In Section 4, we compare the values obtained through different imaging techniques and from different map domains (photon and electron).

The inferred extent of the acceleration region ($\sim$ 16 arcsec) is approximately two-thirds of the total length of the loop. This suggests that the standard model of solar flares where electrons are initially accelerated at a reconnection site near/above the loop top (e.g., Kopp & Pneuman 1976) is not appropriate for certain types of flares. In such flares, the acceleration instead takes place over a large region inside the flare loop.

2. RHESSI Visibilities and Imaging Processes

Solar flare hard X-ray emission is principally produced by accelerated electrons through the bremsstrahlung process (Brown 1971). The relation between the mean electron flux spectrum $\overline{F}(x, y; E)$ (electrons cm^{-2} s^{-1} keV^{-1}), averaged over the line-of-sight direction z through the point (x, y) in a target source, and the corresponding bremsstrahlung hard X-ray spectrum $I(x, y; \epsilon)$ (photons cm^{-2} s^{-1} keV^{-1} arcsec^{-2}) emitted per unit area of the source, can be written as (Piana et al. 2007)

$$I(x, y; \epsilon) = \frac{a^2}{4\pi R^2} \int_{E=\epsilon}^{\infty} N(x, y)\, \overline{F}(x, y; E)\, Q(\epsilon, E)\, dE, \tag{1}$$

where $a = 7.25 \times 10^7$ cm arcsec^{-1}, representing the extent of a one arcsec source at a distance $R = 1$ AU; $Q(\epsilon, E)$ (cm^2 keV^{-1}) is the bremsstrahlung cross-section for emission of a photon at energy ϵ; and $N(x, y)$ (cm^{-2}) is the column density along the line-of-sight direction.

By recording the temporal modulation of the detected flux passing through sets of rotating absorbing grids, *RHESSI* (Lin et al. 2002) encodes imaging information in terms of a set of spatial Fourier components of the source, termed *visibilities*, distributed over nine circles in the spatial frequency (u, v) plane. We define the *count visibility spectrum* $V(u, v; q)$ (counts cm^{-2} s^{-1} keV^{-1}) as the two-dimensional spatial Fourier transform of the count spectrum image $J(x, y; q)$ (counts cm^{-2} s^{-1} keV^{-1} arcsec^{-2}). Similarly, the *electron flux visibility spectrum* $W(u, v; E)$ (electrons cm^{-2} s^{-1} keV^{-1}) represents the two-dimensional spatial Fourier transform of the line-of-sight-column-density-weighted mean electron flux image $N(x, y)\, \overline{F}(x, y; E)$ (electrons cm^{-4} s^{-1} keV^{-1}).

The relation between the observed count visibility spectrum $V(u, v; q)$ and the electron flux visibility spectrum $W(u, v; E)$ is (Piana et al. 2007):

$$V(u, v; q) = \frac{1}{4\pi R^2} \int_{q}^{\infty} W(u, v; E)\, K(q, E)\, dE. \tag{2}$$

Here the kernel $K(q, E)$ satisfies

$$K(q, E)\, dq = \int_{\epsilon=q}^{\infty} D(q, \epsilon)\, Q(\epsilon, E)\, d\epsilon\,, \tag{3}$$

where $D(q, \epsilon)$ is the detector response matrix.

In order to invert Equation (2) to obtain the electron flux visibility spectrum $W(u, v; E)$ from the observed count visibility spectrum $V(u, v; q)$, we employed a Tikhonov regularization technique, which has been proven to be a robust and effective inversion method that results in visibilities (and so images) that vary smoothly with electron energy E. Then from either photon or electron visibility sets, we produce the corresponding images using the visibility-forward-fit, maximum entropy and the uv-smooth interpolation/extrapolation method, as described in Sections 2.1 through 2.3, respectively.

2.1. Visibility-based Forward-fit Algorithm

The visibility-based forward-fit (FWD) imaging algorithm (Schmahl et al. 2007) assumes a parametric source form and determines the values of the model parameters that result in the best fit to the visibility data. This method provides not only quantitative values of the parameters but also their uncertainties. Although the applicability of the FWD algorithm rapidly deteriorates for complex flare morphologies, because of the relatively large number of parameters required to characterize the source structure adequately, the FWD approach is rather effective for sources with a relatively simple structure such as the one we study here.

The FWD routines embedded in the *RHESSI* SolarSoftWare (SSW) provide four simple parametric source geometries: a circular-Gaussian-distributed single source, multiple Gaussian sources, an elliptical-Gaussian source, and a curved-elliptical-Gaussian loop (Hurford et al. 2002; Schmahl et al. 2007). Since the flare we are analyzing has a simple loop-structured geometry, we adopt the curved elliptical Gaussian form. One of the parameters determined by this routine is the FWHM, which for a Gaussian profile, is related to the standard deviation σ by $\exp[-(FWHM/2)^2/2\sigma^2] = 1/2$, i.e., $\sigma = FWHM/\sqrt{8\ln 2}$.

We applied this method to visibility data in both the photon and electron domain to obtain values $\sigma(\epsilon)$ and $\sigma(E)$. Due to the fact that photons of energy ϵ are produced by electron of all energies $E \geq \epsilon$, these two standard deviations are not the same; indeed, one expects in general $\sigma(\epsilon = E) > \sigma(E)$ (see equations [7] and [9] below).

2.2. Maximum Entropy Method

The basis of the Maximum Entropy Method is to maximize the information entropy while minimizing the χ^2 of fit and maintaining the correct value of the total flux. In the MEM-NJIT method (Bong et al. 2006), the visibility amplitudes V are used to calculate the overall flux of the map. The method implements a statistical regularization method where the functional

$$J = H - \alpha\chi^2; \qquad H = -\sum_j^{n_{pix}} \frac{I_j}{\sum_j^{n_{pix}} I_j} \log\left(\frac{I_j}{\sum_j^{n_{pix}} I_j}\right); \qquad \chi^2 = \sum_{l=1}^{n_{vis}} \frac{|V_l - V_l'|}{\sigma_l^2} \tag{4}$$

is minimized by means of an iterative scheme.

In these equations, I is the X-ray image made of n_{pix} pixels, V and V' are the observed and predicted visibilities, respectively, and the σ denote the standard deviations associated with each visibility. The regularization parameter α is obtained by means of optimization techniques. The MEM algorithm implemented in SSW (Bong et al. 2006) provides reliable reconstructions in the case of compact events, although the method often super-resolves the sources and can present convergence problems.

2.3. Fourier-based UV-Smooth Imaging

An alternative visibility-based imaging method, termed the *uv-smooth* (UVS) algorithm, has been recently developed by Massone et al. (2009) and is available on the SSW tree. This method first interpolates the sparsely distributed visibilities to generate a smooth continuum of Fourier components in the spatial-frequency (u, v) plane. Then it performs an FFT-based constrained iterative algorithm to obtain out-of-band extrapolations. The method has proven to reproduce the realistic forms of the sources with a high degree of accuracy, fidelity, robustness, and computational efficiency. Although the method may introduce artifacts when applied to source configurations characterized by distant footpoints, uv-smooth is very accurate when reconstructing relatively localized extended sources.

Unlike images produced by the FWD algorithm, the UVS and MEM procedures do not straightforwardly provide quantitative information on the uncertainties in the determined source extents. Given the electron flux $\overline{F}(x, y; E)$ in a two-dimensional flux image at any given energy E, the *location* of the source can be estimated by calculating the first normalized moment of the intensity. The standard-deviation-based extents (length and width) of the source, in the photon and electron domains respectively, can be found by considering the pertinent second normalized moments:

$$\sigma(\theta;\epsilon) = \sqrt{\frac{\int_0^\infty s^2 I(s,\theta;\epsilon)\, ds}{\int_0^\infty I(s,\theta;\epsilon)\, ds}}, \qquad \sigma(\theta;E) = \sqrt{\frac{\int_0^\infty s^2 N(s)\, \overline{F}(s,\theta;E)\, ds}{\int_0^\infty N(s)\, \overline{F}(s,\theta;E)\, ds}}, \tag{5}$$

where (s, θ) are polar coordinates in the plane of the sky, relative to an origin that we define as the location of the maximum flux intensity. The integrals in Equation (5) are computed numerically for a variety of θ values. The maximum (minimum) values of $\sigma(\theta)$ can be identified as the length (width) standard deviation. In order to provide the quantitative uncertainties on these values, we applied a Monte Carlo approach in which random noise is added to the visibilities and the resulting images recomputed and reanalyzed. Ten realizations of the source visibilities were used; the standard deviations of these ten results were taken to be the 1σ error of the loop extents.

3. Application to A Loop-Structured Flare

In the standard flare model, thick-target "footpoints" are considered to represent the dominant locations of hard X-ray emission because the coronal magnetic loops through which the energetic particles propagate are generally not dense

enough to stop electrons via Coulomb collisions. Due to the high density of the chromosphere, the hard X-ray structure of footpoint sources typically extends over a very small spatial extent, so that observations with available spatial resolutions cannot directly determine details of the particle acceleration and propagation processes in the bremsstrahlung-emitting region.

However, *RHESSI* has revealed a new class of flares in which the hard X-ray emission is predominantly from the coronal loop itself (Krucker et al. 2008; Veronig & Brown 2004; Sui et al. 2004). For such sources, the corona is not only the location of particle acceleration, but also dense enough to act as a thick target, stopping the accelerated electrons before they can penetrate to the chromosphere. Close investigations of these flares can provide direct information on the electron acceleration and propagation processes in the bremsstrahlung-emitting region.

One of the most closely studied events from this class is the "midnight" flare of 2002 April 14 (Sui et al. 2004; Veronig & Brown 2004; Bone et al. 2007; Xu et al. 2008; Kontar et al. 2011b). The left panel in Figure 1 shows the *RHESSI* count rate profiles for this event in five different energy channels. For its entire duration this flare consists of a simple loop structure viewed "side-on" near the solar limb, as shown in the right panel. The coronal loop has a density sufficiently high ($n \simeq 10^{11}$ cm^{-3}, Veronig & Brown 2004) to stop electrons up to ~ 30 keV over the observed loop length of 10^9 cm. It has also been suggested (Kontar et al. 2011b) that electrons must be continuously accelerated during this event because for such a dense loop 20 keV particles have collisional lifetimes less than 0.1 second.

We have analyzed both the photon flux maps and mean electron flux maps for five different time intervals (00:02-00:04, 00:04-00:06, 00:06-00:08, 00:08-00:10, and 00:10-00:12 UT on 2002 April 15) and ten 2-keV energy bins from 10-12 keV up to 28-30 keV. Figure 2 shows the mean electron flux maps at time interval 00:06 - 00:08 UT, obtained through FWD, MEM-NJIT and UVS procedures, all using the electron visibilities obtained through spectral inversion of the observed count visibility data (Piana et al. 2007). All three methods reveal the flare structured as a single loop throughout the studied energy bins. It is to be noted that MEM-NJIT tends to underestimate the source sizes. This behavior has also been shown by Massone et al. (2009) by means of synthetic visibilities simulated according to plausible astrophysical conditions. We therefore use only FWD and UVS algorithms for the analysis to follow.

For the FWD imaging process we adopt a curved-elliptical-Gaussian model, for which the loop geometry is modeled by seven parameters (Xu et al. 2008). One of these seven fitting parameters, i.e., the source extent parallel to the curved arc and termed as the length of the loop L, is particularly important to this study. For the UVS maps, the loop length is estimated from calculating the second normalized moment of the flux intensity using Equation (5). Figures 3 and 4 show the lengths of the source as a function of photon energy ϵ and electron energy E for five given time intervals throughout the peak of the flare. The loop lengths clearly grow with energy. In the "tenuous acceleration region" model of Xu et al. (2008), the form of $L(\epsilon)$ is

$$L(\epsilon) = L_0 + \alpha\epsilon^2, \tag{6}$$

where $L(\epsilon)$ (arcsec) is the loop length at photon energy ϵ (keV); L_0 (arcsec) is the extent of the acceleration region, and α (arcsec keV^{-2}) is a parameter inversely proportional to the plasma density n in the flare loop:

$$\alpha = \frac{1}{Kn}\frac{(\delta-2)}{(\delta-3)(\delta-4)}. \tag{7}$$

Here $K = 2\pi e^4\Lambda$ (e being the electronic charge and Λ being the Coulomb logarithm) and δ is the spectral index of the injected electron flux (Xu et al. 2008). This model assumes that electrons are accelerated within a tenuous region extending from $[-L_0/2, L_0/2]$ and are injected into a dense external region with uniform density[1]. Employing a similar analysis in the electron domain yields

$$L(E) = L_0 + \beta E^2. \tag{8}$$

where $L(E)$ (arcsec) is the electron loop length at electron energy E (keV) and

$$\beta = \frac{1}{Kn}\frac{1}{(\delta-3)}. \tag{9}$$

Since the emission at photon energy ϵ is a weighted sum of electron flux at energies $E \geq \epsilon$, the overall loop extents in the photon domain (Figure 3) are generally larger[2] than those in the electron domain (Figure 4).

By fitting the spatially integrated *RHESSI* X-ray spectra with an isothermal plus collisional thick-target nonthermal model (Brown 1971), we have found that the transition energy between themal and nonthermal components is about 15 keV during this event. Therefore, we fit the acceleration model in the electron domain (equation [8]) starting from $E = 14$ keV. Considering that nonthermal electrons with higher energies contribute substantially to the radiation of thermal photon with lower energies, we fit the visibilities in the photon domain (equation [6]) from $\epsilon = 10$ keV upwards. The fits of the above models, equations [6] and [8], are presented in Figure 3 and 4 respectively. The best-fit acceleration

[1] Note that a more correct "dense acceleration region" form for $L(\epsilon)$, which incorporates emission from the acceleration region itself, exists (Xu et al. 2008). The pertinent form of $L(E)$ is more difficult to use in a best-fit analysis; however, this model yields results for L_0 and n that are very similar to the more straightforward-to-apply "tenuous acceleration region" result (6).

[2] From Equations [6] and [8], the ratio of the propagation lengths is $\alpha\epsilon^2/\beta E^2 = ([\delta-2]/[\delta-4]) \times (\epsilon/E)^2$.

Table 1. Acceleration region length L_0 (Equations [6] and [8]), loop width W and volume V_0(Equation [10])

Time	(hh:mm)	00:02-00:04	00:04-00:06	00:06-00:08	00:08-00:10	00:10-00:12
Photon Map						
L_0 (FWD)	(arcsec)	15.9 ± 0.6	14.8 ± 0.4	15.8 ± 0.5	17.1 ± 0.4	17.8 ± 0.3
L_0 (UVS)	(arcsec)	14.9 ± 0.6	15.3 ± 0.5	16.3 ± 0.4	17.1 ± 0.4	17.2 ± 0.5
W (FWD)	(arcsec)	7.1 ± 1.1	8.6 ± 1.0	8.1 ± 0.8	7.1 ± 0.6	6.8 ± 0.5
W (UVS)	(arcsec)	7.0 ± 1.5	7.5 ± 1.3	7.7 ± 1.5	6.6 ± 1.3	7.3 ± 1.1
V_0 (FWD)	(100 arcsec^3)	6.3 ± 1.9	8.6 ± 2.0	8.2 ± 1.7	6.8 ± 1.2	6.4 ± 0.8
V_0 (UVS)	(100 arcsec^3)	5.7 ± 2.4	6.8 ± 2.4	7.6 ± 3.0	5.9 ± 2.2	7.3 ± 2.2
Electron Map						
L_0 (FWD)	(arcsec)	15.9 ± 0.9	13.3 ± 0.8	16.3 ± 0.9	17.4 ± 0.8	18.3 ± 0.6
L_0 (UVS)	(arcsec)	15.7 ± 0.7	14.7 ± 0.8	16.5 ± 0.6	17.0 ± 0.9	18.1 ± 0.6
W (FWD)	(arcsec)	5.8 ± 1.5	7.8 ± 1.5	7.4 ± 1.3	6.5 ± 0.8	6.2 ± 0.6
W (UVS)	(arcsec)	7.7 ± 1.8	7.1 ± 1.5	7.4 ± 1.7	7.0 ± 1.6	7.6 ± 1.6
V_0 (FWD)	(100 arcsec^3)	4.2 ± 2.2	6.4 ± 2.4	6.9 ± 2.6	5.7 ± 1.5	5.5 ± 1.0
V_0 (UVS)	(100 arcsec^3)	7.3 ± 3.4	5.8 ± 2.5	7.1 ± 3.2	6.5 ± 3.1	8.1 ± 3.4

region extents L_0, obtained using both FWD and UVS methods for each time interval, are shown in Table 1. For each time interval, we have also estimated the loop width W averaged over different energies. Assuming W is the approximate extent of the acceleration region across the magnetic loop and the loop is essentially a cylindrical column, we obtain the volume of the acceleration region to be

$$V_0 = \pi W^2 {L_0}^2/4. \tag{10}$$

The values of W and V_0 are also shown in Table 1. From these results, it can be deduced that:

- the models describe the data accurately in all contexts: both the photon and electron source lengths are well-fit by a quadratic form, with similar values of L_0 in both cases;
- the electron maps generally offer a better fit (i.e., the χ^2 values are smaller), particularly using the FWD procedure. This is primarily due to the regularizing constraints involved in the method used in their construction.

4. Interpretation of the Results

It is often postulated that electrons are accelerated at a reconnection current sheet and that the acceleration process is decoupled from the electron transport that follows the reconnection (Aschwanden 1998). Indeed, many solar flares demonstrate a clear loop-top-plus-footpoints structure (see, e.g., Battaglia & Kontar 2011). However, the spatially resolved observations presented here instead suggest the presence of an extended acceleration site inside the loop. Further, given that the acceleration region is estimated to be a substantial fraction of the total length of the flare loop ($\sim 30''$; see Figures 3 and 4) and that the hard X-ray emission is produced in the entire loop instead of only at the footpoints, it is clear that the dense flare loop incorporates both acceleration and transport of electrons, with concurrent thick-target bremsstrahlung emission. The kinetic energy of most of the electrons is lost due to collisional interactions with ambient plasma before the electrons can reach the chromosphere.

Such a scenario is consistent with the presence of an enhanced level of MHD fluctuations inside the loop (Bian et al. 2011). It is possible that for such events reconnection and loop-top injection may not correspond to the dominant energy dissipation and particle acceleration process, which instead may proceed inside the flare loop itself through stochastic mechanisms (Petrosian & Liu 2004). Our result shows that a considerable proportion of the flare loop is involved in the process of acceleration, thus avoiding the "number problem" (Brown et al. 2009).

5. Conclusions

We have analyzed an extended coronal hard X-ray source in the event of 2002 April 14 with photon maps constructed from count visibilities (two-dimensional spatial Fourier transforms of the source geometry). Furthermore, using a regularized spectral inversion technique generating electron visibilities, we have studied the variation of the electron flux image with electron energy E. The source extents from both photon and electron maps generally grow quadratically with energy, in agreement with a collisional model involving an extended acceleration region (Xu et al. 2008; Kontar et al. 2011b; Bian et al. 2011). Fitting this model allows estimation of the length and volume of the acceleration region: ~ 16 arcsec and ~ 600 arcsec^3. We compare the results obtained by different algorithms (FWD and UVS) and from both photon and electron visibility domains. The plausible and consistent estimates of the loop structures and acceleration-region sizes strongly suggest the proposed model to be theoretically reliable and the visibility-based imaging methods to be robust and faithful.

Detailed studies of more cases of dense-loop flares will be carried out in future work. We will also focus our attention to variation of the second dimension of the loop – the loop width W – with electron energy in order to gain a better understanding of cross-field transport processes (Kontar et al. 2011b) and properties of MHD turbulence in solar flare acceleration sites (Bian et al. 2011).

Acknowledgements. The authors are very grateful to Richard Schwartz, Kim Tolbert, Gordon Hurford, Iain Hannah and Yan Xu for useful *RHESSI* techniques and fruitful discussions. The work is supported by STFC Rolling grant and the EU FP7 HESPE grant no. 263086; AGE was supported by NASA Grant NNX10AT78J.

References

Aschwanden, M. 1998, ApJ, 502, 455
Battaglia, M. & Kontar, E. P. 2011, ApJ, 735, 42
Bian, N. H., Kontar, E. P., & MacKinnon, A. L. 2011, A& A, 535, A18
Bone, L., Brown, J. C., Fletcher, L., Veronig, A., & White, S. 2007, A&A, 466, 339
Bong, S.-C., Lee, J., Gary, D. E., & Yun, H. S. 2006, ApJ, 636, 1159
Brown, J. 1971, Sol. Phys., 18, 489
Brown, J. C., Turkmani, R., Kontar, E. P., MacKinnon, A. L., & Vlahos, L. 2009, A&A, 508, 993
Emslie, A. G., Kontar, E. P., Krucker, S., & Lin, R. P. 2003, ApJL, 595, L107
Holman, G. D., Aschwanden, M. J., Aurass, H., et al. 2011, Space Sci. Riew., 159, 107
Hurford, G. J., Schmahl, E. J., Schwartz, R. A., et al. 2002, Sol. Phys., 210, 61
Kontar, E. P., Brown, J. C., Emslie, A. G., et al. 2011a, Space Sci. Rev., 159, 301
Kontar, E. P., Hannah, I. G., & Bian, N. H. 2011b, ApJL, 730, L22
Kopp, R. A. & Pneuman, G. W. 1976, Sol. Phys., 50, 85
Krucker, S., Battaglia, M., Cargill, P., et al. 2008, A& A Review, 16, 155
Lin, R., Dennis, B., Hurford, G., et al. 2002, Sol. Phys., 210, 3
Massone, A. M., Emslie, A. G., Hurford, G. J., et al. 2009, ApJ, 703, 2004
Petrosian, V. & Liu, S. 2004, ApJ, 610, 550
Piana, M., Massone, A. M., Hurford, G. J., et al. 2007, ApJ, 665, 846
Schmahl, E. J., Pernak, R. L., Hurford, G. J., Lee, J., & Bong, S. 2007, Sol. Phys., 240, 241
Sui, L., Holman, G. D., & Dennis, B. R. 2004, ApJ, 612, 546
Veronig, A. & Brown, J. 2004, ApJL, 603, L117
Xu, Y., Emslie, A. G., & Hurford, G. J. 2008, ApJ, 673, 576

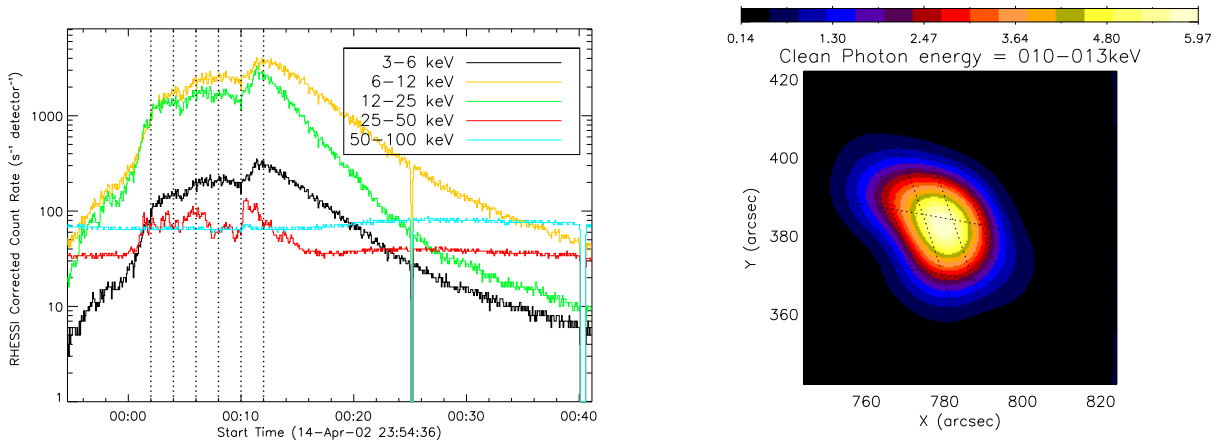

Fig. 1. *Left:* Time profile in different *RHESSI* energy ranges of the flare starting around 23:55 UT on 2002 April 14. The vertical lines indicate the time duration for which the spectral fitting and visibility-based imaging were performed. *Right:* An example of a photon flux map (for the time interval 00:05 - 00:10 UT and energy bin 10-13 keV) obtained by the Clean method (Hurford et al. 2002).

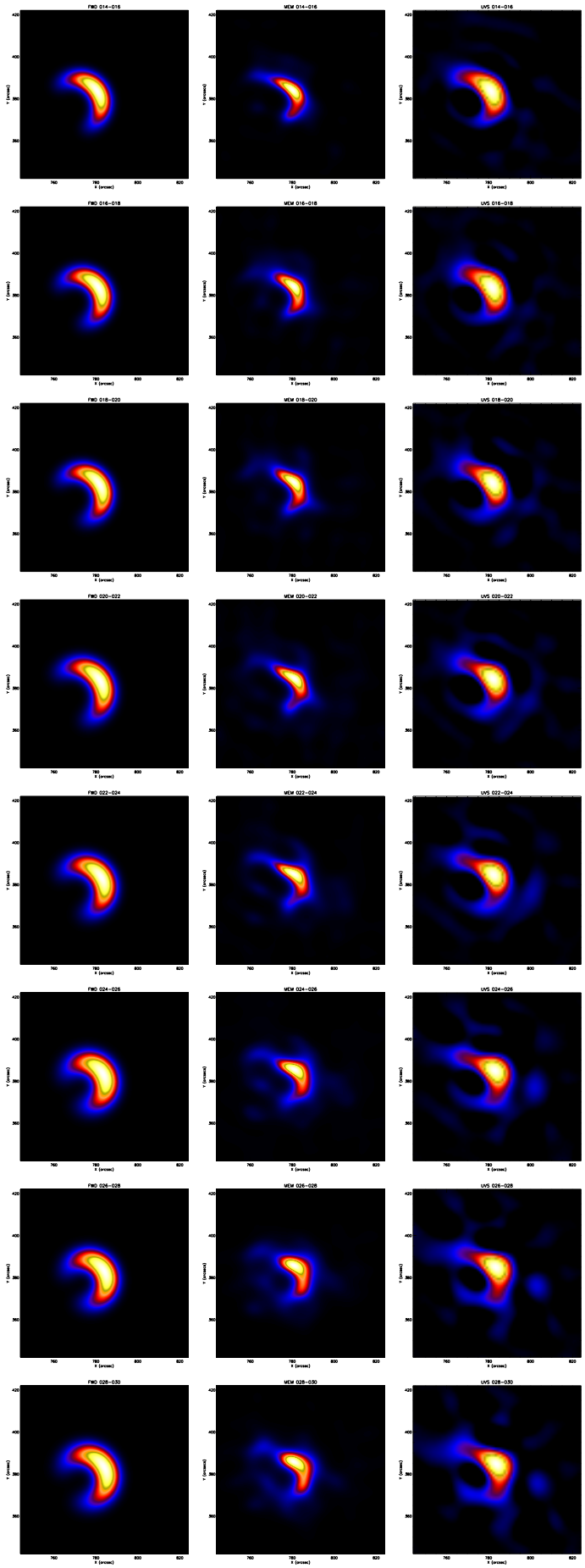

Fig. 2. Mean electron flux maps for the time interval 00:06 - 00:08 UT, obtained through visibility-forward-fit (*left*), Maximum Entropy (MEM-NJIT) (*middle*) and uv-smooth (*right*) procedures applied to electron visibilities. Energy bins are from 14-16 keV (*top*) to 28-30 keV (*bottom*).

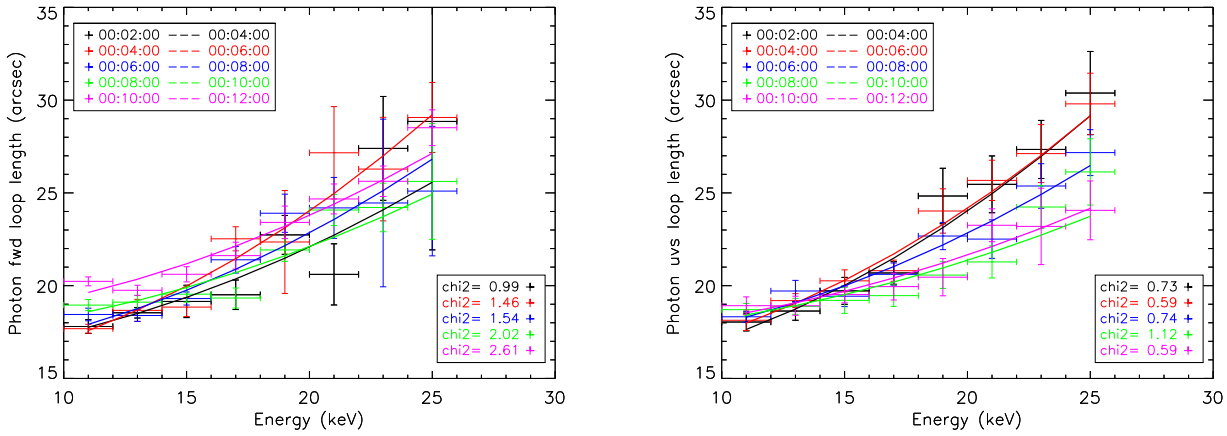

Fig. 3. Flare loop lengths for each 2-keV photon energy bins, for five different time intervals. *Left:* results from forward-fit algorithm; *right*: results from uv-smooth method. The solid curves represent the fits of the model described in Equation (6). The χ^2 of the fittings are also shown.

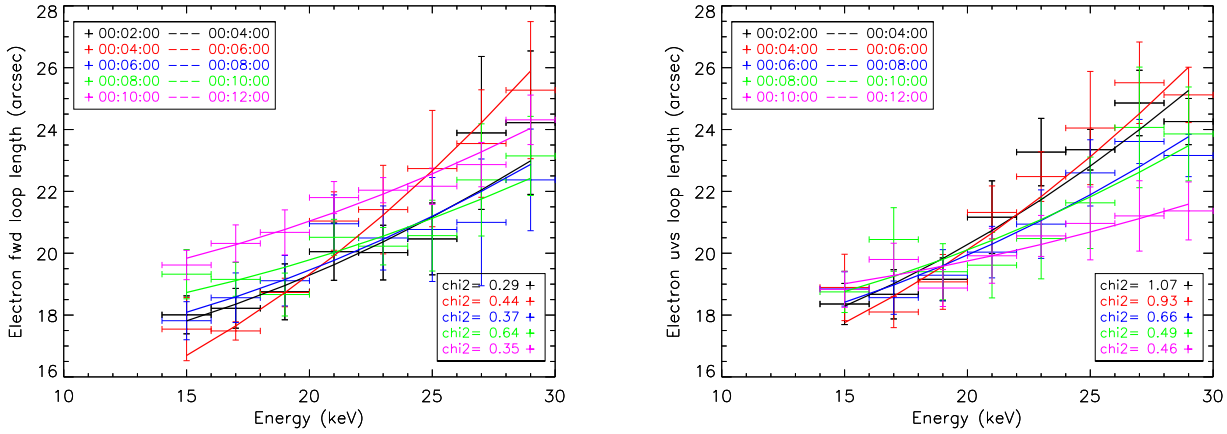

Fig. 4. Flare loop lengths for each 2-keV electron energy bin, for the same five time intervals as in Figure 3. *Left:* results from forward-fit algorithm; *right*: results from uv-smooth method. The solid curves represent the fits of the model described in Equation (8). The χ^2 of the fittings are also shown.